

---

# Learning dynamic image representations for self-supervised cell cycle annotation

---

Anonymous Authors<sup>1</sup>

## Abstract

Time-based comparisons of single-cell trajectories passing through cell cycle are challenging due to their intrinsic heterogeneity, autonomous decisions, dynamic transitions and unequal lengths. In this paper, we present a self-supervised framework combining an image autoencoder with dynamic time series analysis of latent feature space to represent, compare and annotate cell cycle phases across single-cell trajectories. In our fully data-driven approach, we map similarities between heterogeneous cell tracks and generate statistical representations of single-cell trajectory phase durations, onset and transitions. This work is a first effort to transform a sequence of learned image representations from cell cycle-specific reporters into an unsupervised sequence annotation.

## 1. Introduction & Background

During its lifetime, a cell passes through a series of well-characterised, morphologically distinct cycling stages that prepare it to divide (Fig.1, App.A). Quantitative cell cycle analysis is an essential tool for understanding cell behavior and dynamics of their growth and division. In recent years, multigenerational lineage tracing has enabled measuring cell behavior at the single-cell level over time. However, accurate identification and labeling of cell cycle phases dynamics along trajectories with variable durations remains challenging as it requires meaningful interpretation of low-resolution signals that vary continuously over time (Fig.1).

In this paper, we use the cell cycle phases as an exemplar to present a novel, supervision-free approach for automated representation, comparison and annotation of continuous processes along single-cell trajectories. Our data-driven trajectory analysis is based on (i) self-supervised extraction of latent features from cell cycle-specific image data and (ii) inference of phase labels via parameter-free dynamic time warping (DTW) from a miniature annotated cell library.

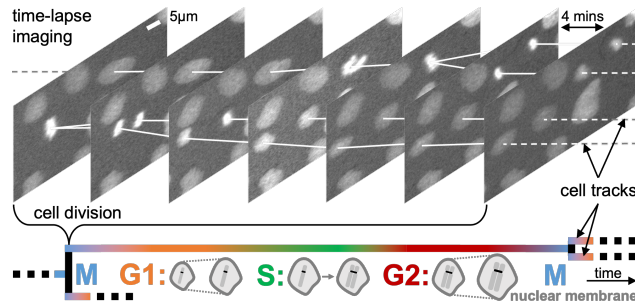


Figure 1. The objective to annotate continuous measurements, such as cell cycle phases, in single-cell trajectories from raw time-lapse image data capturing cell cycle-specific reporter dynamics over the Growth, Synthesis and Mitotic phases of variable lengths.

Previous analyses addressing the morphodynamic transition challenges have sourced from latent image representations, however, these methods either rely on compressing the entire trajectory with variable durations into single, fixed-length embedding (Wu et al., 2022), or truncate the time-resolved tracks to an identical, pre-defined length (Soelistyo et al., 2022). Conversely, the length-invariant approaches are either driven by hand-crafted features (El-Labban et al., 2014) or yield poorly interpretable continuous latent space clustering (Ji et al., 2017), which complicates discrete categorical cell cycle phase annotation (Rappé et al., 2020).

Our approach contributes to the associated challenges of cell cycle phase labeling three-fold. First, our cell-specific image autoencoder learns compressed latent representations of individual cell images and captures key instantaneous features of a cell cycle-specific reporter. This step addresses the difficulty of quantifying low-resolution signals and compensates for complicated feature hand-crafting. Second, the sequence of image-specific latent space embeddings is employed to localise regions of (dis-)similarity between two trajectories by dynamic matching. We leverage this self-supervised strategy to infer phase labels of an unseen trajectory from an annotated cell library to categorically label cell phases. This automated labeling step allows time-based comparisons in the context of entire trajectories of unequal lengths. Third, extending beyond categorical labeling, our approach enables the quantitative statistical representation of label distribution in cell trajectories for a supervision-free annotation of new data, enriched with an uncertainty measure. We challenge the concept of categorical labeling of continuous processes by proposing a flexible, more appropriate alternative.

<sup>1</sup>Anonymous Institution, Anonymous City, Anonymous Region, Anonymous Country. Correspondence to: Anonymous Author <anon.email@domain.com>.

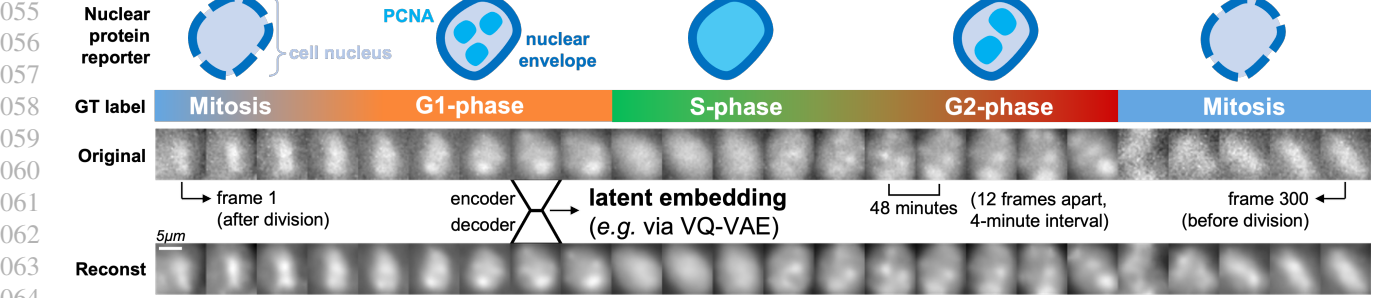


Figure 2. Characteristic PCNA morphology throughout the cell cycle. Hand-annotated phases and transitions along an original single-cell image sequence with corresponding encoded-decoded *VQ-VAE* reconstructions, capturing key image features in form of latent embeddings. These include coarse information, such as cell nucleus size and shape, with detailed patterns of reporter signal distribution.

## 2. Methods & Workflow

### 2.1. Live-cell imaging & single-cell trajectory dataset

The image dataset was acquired by automated time-lapse microscopy via live-cell fluorescence imaging of Madin–Darby canine kidney (MDCK) epithelial cells (Bove et al., 2017), expressing both *H2b-GFP* (constitutive histone marker for nuclei detections) and *PCNA-iRFP* (cell cycle phase-specific protein with morphological transitions) reporter systems.

The cells were segmented (Weigert et al., 2020), classified (Ulicna et al., 2022) and tracked (Ulicna et al., 2021) to reconstruct multi-generational lineage trees (Fig.1). Single-cell trajectories had their image patches centered at the cell nucleus along the track and cropped at  $\approx 10 \times 10 \mu\text{m}$  scale (Fig.2, App.B). The complete, hand-annotated dataset consists of 204 fully-resolved single-cell trajectories from 4 movies, divided into 35 reference vs. 169 query cell tracks.

### 2.2. Latent image representation learning with *VQ-VAE*

The *VQ-VAE* architecture (Oord et al., 2018) is formed of a convolutional *encoder* which compresses an original image  $x$  into a lower-dimensional representation  $z_e(x)$ , which is then *quantized* by a nearest neighbour look-up, or  $\ell_2$  norm, along the channel dimension to a latent embedding space “codebook” (Fig.3). The quantized discrete embeddings  $z_q(x)$  are then passed through a convolutional *decoder* to

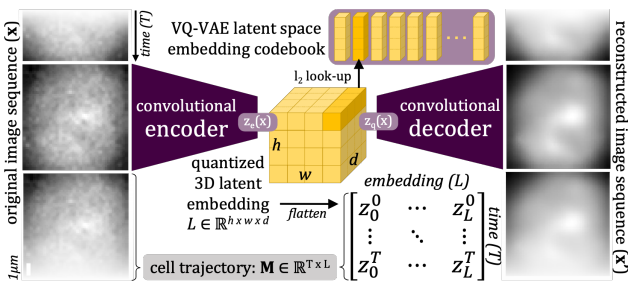


Figure 3. Latent representation learning. *VQ-VAE* is trained to learn a low-dimensional image representation from single-cell image patches. The entire trajectory is represented as  $M \in \mathbb{R}^{T \times L}$ .

produce the reconstruction image  $x'$ . All downstream analysis uses the flattened  $L$ -dimensional representation, where  $L \in \mathbb{R}^{h \times w \times d}$ , i.e. the quantized latent embedding dimensionality. These are extracted per-image along the entire trajectory order of  $T$  time points in length (Fig.3, App.B).

### 2.3. Dynamic time warping of trajectory latent features

Latent feature embeddings are extracted from a pair of arbitrarily long reference and query image sequences to compute a dynamic warping matrix using  $\ell_2$  distance (Fig.4). The warping matrix is traversed by backward algorithm (Berndt & Clifford, 1994) to identify and locate the minimum-cost alignment path used to infer trajectory phase annotations from the hand-annotated reference cell. Guided by the alignment path, each unannotated query cell position is mapped to the reference cell position to which it warps closest and copies the corresponding reference label (Fig.4, App.C).

### 2.4. Evaluation of categorical phase annotation fidelity

Each “inferred” categorical annotation (from single reference or most common overlap across  $N$  references, Fig.5) is contrasted to hand-annotated ground truth (GT) via intersection over union score as  $IoU_{phase} = \frac{TP}{TP+FP+FN}$ , where the  $TP$  (true +) are instances where the position’s predicted label matches GT, whilst the  $FP$  (false +) covers instances where predicted label is not in GT, and the  $FN$  (false –) covers instances where label is in GT but misses in prediction. The overall  $IoU_{total} = \frac{TP+TN}{TP+TN+FP+FN}$  score reflects the ratio of correct detections (true + and –) to all detections (i.e. sequence agreement or accuracy, Fig.5).

## 3. Experiments & Results

### 3.1. Motivation behind individual steps of the workflow

This section deploys image latent encodings to perform dynamic time warping between two sequences, allowing the cell cycle phase annotation. Importantly, we aim to highlight the versatility of our workflow which is agnostic to the choice of a feature extractor (§3.2), including pre-trained

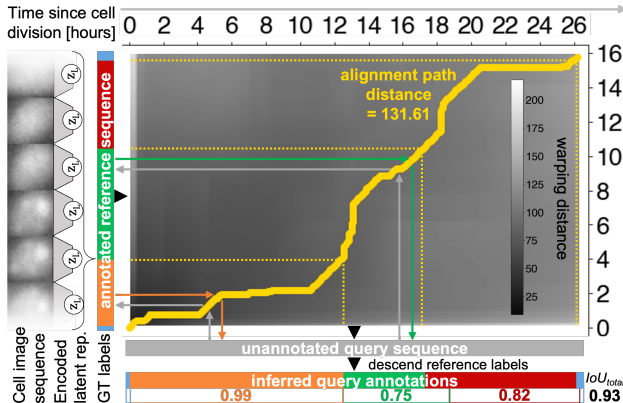


**Figure 4. Supervision-free reference-guided labelling of query trajectories with dynamic time warping of latent representations.** The VQ-VAE-encoded latent embeddings (left) from both reference and query image sequences are warped to compute their best alignment path (thick yellow line) from the warping matrix. Query phase labels (horizontal bars) are inferred from the path (arrows) and follow the categorical labels from a hand-annotated reference (vertical bar). Scores reflect overlap with GT annotation.

“off-the-shelf” models or hand-crafted features. Although model explainability is beyond the scope of this work, we implemented an image autoencoder (§2.2) with a motivation to learn *meaningful* latent embeddings which can be verified through image reconstructions (Fig.2). Additionally, custom-trained models allow for latent space dimensionality control, which can be optimised and/or experimented with.

The DTW approach choice (§2.3) could also be substituted by simpler supervision-free methods, such as search for closest image embedding from the reference library on per-image basis without considerations of the time flow. This strategy, however, yields noisy annotations with frequent back-and-forth flipping between states. Such noise, concentrated at phase transitions, is difficult to clean and disables reliable sequence partitioning into cell cycle phase regions.

Approaching the problem with a hidden Markov model (HMM) also poses conceptual limitations as the *Markov property* dictates that the future state depends only on the present state and not on past history. In the cell cycle, however, certain events (*e.g.* checkpoint passing; G1) need to

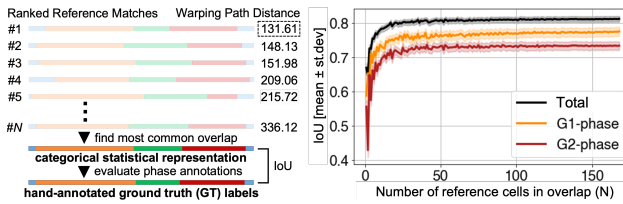


**Figure 5. Improving annotation fidelity by considering  $N$  reference sequences** and finding most common overlap per each trajectory position. Such “categorical statistical representation” is evaluated against GT hand-annotations (left). IoU scores (35 queries) initially improve but saturate at  $N \approx 20$  references (right).

occur prior to others (*e.g.* DNA replication; S), following an orchestrated and deterministic chronology, which the “memoryless” and stochastic HMM cannot faithfully model.

HMM represents transitions purely statistically, with the state changes guided by (known) transition probabilities. Not only does this homogenise the variable phase lengths in trajectories, but calculating such probabilities requires input of prior knowledge of the modelled system. Unlike HMMs, the supervision-free DTW finds structure by establishing a memory of cell cycle event order as it monitors event flow over time in the context of whole trajectory, which extends its utility to cases where phase durations are variable (§3.2).

### 3.2. Phase annotation with real & distorted trajectories

To evaluate our supervision-free annotation methodology, we initially focused on track instances where the overall length of the two trajectories is different and the relative duration of the individual cell cycle phases to the whole trajectory also differs. Using a representative trajectory pair, we confirm the high performance of our strategy (Fig.4).

To increase the representational power of each annotation to more references, we inferred the phase labels for 35 different query cells by warping each cell to 169 references. To evaluate how many references are needed to provide reliable annotation, we sampled  $N$  random references and generated a categorical statistical representation (Fig.5). Initially, adding more references significantly improves the fidelity of cell phase labeling, but eventually reaches a point where annotations are not improved nor worsened. This “saturation point” appears with as little as 20 references for overall and phase-specific scores (Fig.5). Whilst recognising that other less reproducible and more stochastic processes could express higher dependency on data quantity, this result hints towards the potential scalability of our approach with larger reference libraries, and to implementations in other time-resolved systems where labeled data availability is sparse.

To extend our technology’s potential to annotate other dynamic processes in cell trajectories, we tested the importance of our cell-specific VQ-VAE feature extractor. To benchmark its performance, we replaced the VQ-VAE encoder with a custom-trained  $\beta$ -VAE model (Higgins et al., 2017) and an IMAGENET pre-trained RESNET-18 network (He et al., 2015) (App.B). Annotating 169 unseen trajec-

**Table 1.** Phase labelling accuracy of 169 query cells warped against 35 reference cells annotated via most common overlap strategy with image latent embeddings from various deep feature extractors.

	<i>IoU score</i>	RESNET-18	$\beta$ -VAE	VQ-VAE
M	<b><math>0.83 \pm 0.12</math></b>	$0.79 \pm 0.12$	$0.78 \pm 0.13$	
G1	$0.73 \pm 0.21$	$0.70 \pm 0.20$	<b><math>0.74 \pm 0.17</math></b>	
S	$0.55 \pm 0.18$	$0.50 \pm 0.23$	<b><math>0.59 \pm 0.17</math></b>	
G2	$0.69 \pm 0.15$	$0.68 \pm 0.16$	<b><math>0.70 \pm 0.14</math></b>	
<b>TOTAL</b>	$0.78 \pm 0.10$	$0.75 \pm 0.13$	<b><math>0.79 \pm 0.10</math></b>	

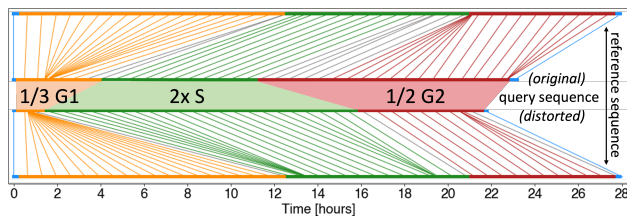
165 stories with inferred overlaps across 35 reference cells, we  
 166 reveal that our *VQ*-VAE-extracted embeddings yield high  
 167 annotation fidelity but are interchangeable with other image  
 168 feature extractors, confirming the versatility of our approach  
 169 (Table 1). Conversely, warping the trajectories based on  
 170 hand-crafted features, *e.g.* image intensity or region proper-  
 171 ties, suffers in performance (data not shown), highlighting  
 172 the importance of deep feature extractors in this task.

173 Next, we investigated if our time-series matching could  
 174 be extended to cases where phase durations deviate from  
 175 expected distributions, such as under pharmacological per-  
 176 turbations which result in evident shortening or prolonging  
 177 of certain cell cycle phases. To overcome the shortage of  
 178 real trajectories with out-of-distribution phase durations in  
 179 our dataset, we synthesized a distorted sequence from a real  
 180 cell trajectory (Fig.6), and contrasted both variants' warping  
 181 pattern against the same trajectory. The dynamic nature of  
 182 the warping successfully matches the phases in both cases  
 183 (Fig.6), extending the potential utility of our methodology  
 184 to cell cycle-targeting pharmacological manipulations.

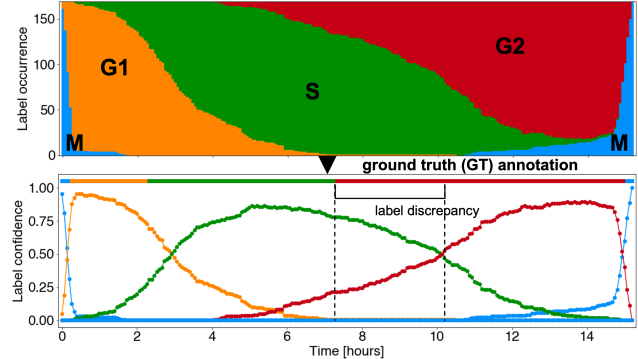
### 186 3.3. Statistical representation of cell phase transitions

188 The continuous nature of PCNA features complicates the  
 189 labelling of the cell cycle into discrete categories upon both  
 190 manual and automated annotation. This is most evident at  
 191 the S/G2 transition which represents a gradual process, un-  
 192 like at the relatively sudden G1/S switch-like change (Fig.2).  
 193 Importantly, our approach recapitulates the human annota-  
 194 tors' (un-)certainty when partitioning the trajectory phase  
 195 regions and can be leveraged to quantify the "label confi-  
 196 dence" score along the entire trajectory (Fig.7). Organizing  
 197 and visualizing the phase annotations of a single query cell  
 198 via warping to 169 reference cells illustrates where phases  
 199 hold a strong majority vote *vs.* regions of phase ambiguity,  
 200 as well as the continuous transitions between them (Fig.7).

202 To express the label confidence with high representational  
 203 power, we compute the frequency of each label, *e.g.* the 1<sup>st</sup>  
 204 trajectory time point has the M-phase inferred 161 out of  
 205 169 times (95%, Fig.7). The illustration of this statistical  
 206 representation can be interpreted as a new, refined cate-



215 **Figure 6. Warping performance on out-of-distribution trajec-  
 216 tories.** The same reference cell (top and bottom) is warped (vertical  
 217 lines, gray if labels mismatch) to two sequences: an original (center  
 218 top) and distorted (center bottom) trajectory, created from every  
 219 3<sup>rd</sup> G1- and every 2<sup>nd</sup> G2- and by duplicating every S-phase frame.



220 **Figure 7. Statistical representation of cell cycle phase anno-  
 221 tations.** Representative sequence label occurrence per time point  
 222 (x-axis) inferred from 169 references (y-axis). Visualisation of la-  
 223 bel confidence, *i.e.* the fraction of label's predicted times, confirms  
 224 the fast onset of the relatively sharp G1/S transition, whilst the  
 225 S/G2 transition occurs more gradually (less defined both intrinsi-  
 226 cally and though PCNA or other reporters), causing a discrepancy  
 227 ( $\approx 2.5$  hours) between the statistically inferred labels and the GT.

228 gorical annotation, which allows us to express numerical  
 229 confidence scores to highlight transitional regions. Notably,  
 230 the per-position label confidence of the cell cycle remains  
 231 above 50% throughout the trajectory, which is twice as high  
 232 as pseudo-random label choice, *i.e.* 25% if selecting 1 out  
 233 of 4 labels completely randomly. In general, the highest  
 234 confidence labels match the GT annotation, except for the  
 235 ambiguous S/G2 transition which is also difficult to hand-  
 236 annotate (Fig.7). This motivates us to challenge the consen-  
 237 sus of categorical phase annotation and raise the importance  
 238 of quantifying the certainty of annotating continuous events.

## 4. Discussion & Conclusions

239 This paper proposes a self-supervised, parameter-free gen-  
 240 eralizable framework to dynamically find similarities in cell  
 241 trajectories based on latent image features. Without incor-  
 242 poration of prior knowledge about typical cell cycle-specific  
 243 characteristics, the cell cycle phase dynamics serve as an ex-  
 244 emplar to quantitatively characterize the continuous nature  
 245 of single-cell trajectory transitions and their rigid labeling.

246 Certain open questions worth investigating include inter-  
 247 pretability of the latent features, *e.g.* via ablations or prun-  
 248 ing to reveal and evaluate the salient features required for  
 249 correct annotation. Our framework, currently bound by need  
 250 for few defined categorical cell labels, enables adaptation to  
 251 other track annotation purposes in a fully data-driven way.

252 Despite its limitations, we envisage the applicability of this  
 253 proposed technology in elucidating the effects of pharma-  
 254 cological perturbations (§3.2) or measuring the dynamics tied  
 255 to other heterogeneous datasets, *e.g.* cell fate determination,  
 256 signalling pathways, morphogen gradients, *etc.* (Shakarchy  
 257 et al., 2023; Gallusser et al., 2023), in biology and beyond.

---

## References

- Berndt, D. J. and Clifford, J. Using dynamic time warping to find patterns in time series. In *KDD Workshop*, 1994. URL <https://dl.acm.org/doi/10.5555/3000850.3000887>.
- Bove, A., Gradeci, D., Fujita, Y., Banerjee, S., Charras, G., and Lowe, A. R. Local cellular neighborhood controls proliferation in cell competition. *Molecular Biology of the Cell*, 28(23):3215–3228, November 2017. ISSN 1059-1524, 1939-4586. doi: 10.1091/mcb.e17-06-0368. URL <https://www.molbiolcell.org/doi/10.1091/mcb.e17-06-0368>.
- Burgess, C. P., Higgins, I., Pal, A., Matthey, L., Watters, N., Desjardins, G., and Lerchner, A. Understanding disentangling in  $\beta$ -vae, 2018. URL <https://arxiv.org/abs/1804.03599>.
- El-Labban, A., Zisserman, A., Toyoda, Y., Bird, A., and Hyman, A. Temporal models for mitotic phase labelling. *Medical Image Analysis*, 18(7):977–988, 2014. ISSN 1361-8415. doi: <https://doi.org/10.1016/j.media.2014.05.003>. URL <https://www.sciencedirect.com/science/article/pii/S1361841514000681>.
- Gallusser, B., Stieber, M., and Weigert, M. Self-supervised dense representation learning for live-cell microscopy with time arrow prediction, 2023. URL <https://arxiv.org/abs/2305.05511>.
- He, K., Zhang, X., Ren, S., and Sun, J. Deep residual learning for image recognition, 2015. URL <https://arxiv.org/abs/1512.03385>.
- Higgins, I., Matthey, L., Pal, A., Burgess, C., Glorot, X., Botvinick, M., Mohamed, S., and Lerchner, A. beta-VAE: Learning basic visual concepts with a constrained variational framework. In *International Conference on Learning Representations*, 2017. URL <https://openreview.net/forum?id=Sy2fzU9gl>.
- Ji, P., Zhang, T., Li, H., Salzmann, M., and Reid, I. Deep subspace clustering networks. *Advances in Neural Information Processing Systems*, 30, 2017. URL [https://proceedings.neurips.cc/paper\\_files/paper/2017/file/e369853df766fa44e1ed0ff613f563bd-Paper.pdf](https://proceedings.neurips.cc/paper_files/paper/2017/file/e369853df766fa44e1ed0ff613f563bd-Paper.pdf).
- Oord, A. v. d., Vinyals, O., and Kavukcuoglu, K. Neural Discrete Representation Learning, May 2018. URL <http://arxiv.org/abs/1711.00937>. arXiv:1711.00937 [cs].
- Rappez, L., Raklin, A., Rigopoulos, A., Nikolenko, S., and Alexandrov, T. DeepCycle reconstructs a cyclic cell cycle trajectory from unsegmented cell images using convolutional neural networks. *Molecular Systems Biology*, 16(10), October 2020. ISSN 1744-4292, 1744-4292. doi: 10.15252/msb.20209474. URL <https://onlinelibrary.wiley.com/doi/10.15252/msb.20209474>.
- Shakarchy, A., Zarfati, G., Hazak, A., Mealem, R., Huk, K., Avinoam, O., and Zaritsky, A. Machine learning inference of continuous single-cell state transitions during myoblast differentiation and fusion. *bioRxiv*, 2023. doi: 10.1101/2023.02.19.529100. URL <https://www.biorxiv.org/content/early/2023/02/19/2023.02.19.529100>.
- Soelistyo, C. J., Vallardi, G., Charras, G., and Lowe, A. R. Learning biophysical determinants of cell fate with deep neural networks. *Nature Machine Intelligence*, 4(7):636–644, June 2022. ISSN 2522-5839. doi: 10.1038/s42256-022-00503-6. URL <https://www.nature.com/articles/s42256-022-00503-6>.
- Ulicna, K., Vallardi, G., Charras, G., and Lowe, A. R. Automated Deep Lineage Tree Analysis Using a Bayesian Single Cell Tracking Approach. *Frontiers in Computer Science*, 3:734559, October 2021. ISSN 2624-9898. doi: 10.3389/fcomp.2021.734559. URL <https://www.frontiersin.org/articles/10.3389/fcomp.2021.734559/full>.
- Ulicna, K., Ho, L. T. L., Soelistyo, C. J., Day, N. J., and Lowe, A. R. Convolutional neural networks for classifying chromatin morphology in live-cell imaging. *Chromosome Architecture: Methods and Protocols*, pp. 17–30, 2022. doi: 10.1007/978-1-0716-2221-6\_3. URL [https://doi.org/10.1007/978-1-0716-2221-6\\_3](https://doi.org/10.1007/978-1-0716-2221-6_3).
- Weigert, M., Schmidt, U., Haase, R., Sugawara, K., and Myers, G. Star-convex polyhedra for 3d object detection and segmentation in microscopy. In *2020 IEEE Winter Conference on Applications of Computer Vision (WACV)*. IEEE, mar 2020. doi: 10.1109/wacv45572.2020.9093435. URL <https://www.computer.org/csdl/proceedings-article/wacv/2020/09093435/1jPbBJZQVZ6>.
- Wu, Z., Chhun, B. B., Popova, G., Guo, S.-M., Kim, C. N., Yeh, L.-H., Nowakowski, T., Zou, J., and Mehta, S. B. DynaMorph: self-supervised learning of morphodynamic states of live cells. *Molecular Biology of the Cell*, 33(6):ar59, May 2022. ISSN 1059-1524, 1939-4586. doi: 10.1091/mbc.E21-11-0561. URL <https://www.molbiolcell.org/doi/10.1091/mbc.E21-11-0561>.

## 275 A. Appendix: The biology of the cell cycle

276 **Cell cycle as a biological phenomenon** In unicellular as well as multicellular eukaryotes, the **cell cycle** is a ubiquitous,  
 277 complex process fundamentally involved in the growth and proliferation of cells and entire organisms. The cell cycle  
 278 represents an essential process governed by the coordination of highly controlled molecular processes. Numerous regulatory  
 279 proteins and signalling pathways unite to direct the cell through a specific sequence of events. These result in the replication  
 280 of the cell's genetic material culminating at cell division, *i.e.* the event of equal partitioning of the cell's genetic material and  
 281 cell splitting into two newly-produced daughter cells.  
 282

283 **Progression through cell cycle phases** The cell cycle can be sub-divided depending on various criteria; the most common  
 284 categorisation groups the *G1*-, *S*-, and *G2*-phases, which together encompass the **interphase** (Figure 8). The interphase is  
 285 the longest phase between subsequent cell divisions defined by cell growth and DNA replication event. Interphase represents  
 286 the portion of the cell cycle that is not accompanied by visible cell changes under the microscope, during which the cell  
 287 partakes in various essential activities:  
 288

- 290 • In the **G1 (Gap / Growth one) phase**, the cell grows and responds to the environmental, biochemical and mechanical  
 291 cues. A high amount of protein synthesis occurs and the cell accumulates nutrients and growth factors as it is about to  
 292 double its original size. More organelles are produced and the volume of the cytoplasm increases.  
 293
- 294 • In the **Synthesis (S) phase**, the cell synthesises its DNA and the amount of DNA is doubled whilst the number of  
 295 chromosomes remains constant (via semi-conservative replication). Concomitantly, some of the organelles, including  
 296 mitochondria, are replicated.  
 297
- 298 • In the **G2 (Gap / Growth two) phase**, the cell resumes its growth in preparation for division. The mitochondria (and in  
 299 plants, also the chloroplasts) divide and the cell continues to grow and accumulate nutrients needed until mitosis begins.  
 300
- 301 • In addition, some cells that do not divide often (*e.g.* hepatocytes, stem cells) or ever (*e.g.* terminally differentiated cells,  
 302 including epidermis, neurons, or muscle cells), enter a stage called **G0 (Gap zero) phase**, which is separate from, or a  
 303 preceding extension of, the interphase. G0 cells are not actively cycling, and are therefore considered to interrupt the  
 304 interphase. In some circumstances, the G0-phase may remain as a distinct quiescent stage which occurs outside of the  
 305 cell cycle. Alternatively, the G0-phase may end and be followed by the remaining stages of interphase.  
 306

307 The periods of interphase that surround the S-phase have historically been named the "gaps" in the cell cycle to separate the  
 308 stages between the two obvious landmarks; the DNA synthesis and mitosis. However, these phases are key periods for cell  
 309 cycle regulation and include the crucial decision to commit to DNA replication during G1, and to initiate the process that  
 310 leads to chromosome segregation during G2. In addition, to ensure that each interphase sub-stage is correctly completed,  
 311 each phase ends when a **cellular checkpoint** validates the accuracy of the stage's completion before proceeding to the next.  
 312 As a quality control mechanism, the cell can decide to undergo apoptosis, which represents a highly regulated cell signalling  
 313 process of biochemical and/or mechanical nature leading to programmed cell death.  
 314

## 315 B. Appendix: Deep image feature extractors

316 **Latent feature extraction** To extract image-based features describing PCNA cell phase morphology using automated  
 317 approaches, cell-centred image patches were cropped from the fluorescence channel microscopy frames using the tracking  
 318 coordinates. To complement manual feature extraction, we intended to learn latent representations of the image patches with  
 319 an autoencoder-driven approach.  
 320

321 **Training image dataset** To train the variational autoencoder-based models, 3 representative movies had  $\approx 50,000$  patches  
 322 randomly extracted. Since not all images expressed the *PCNA-iRFP* channel in sufficient amounts, the PCNA-reconstructing  
 323 models were thus trained on particularly noisy, but representative, dataset.  
 324

### 325 B.1. Vector Quantized Variational AutoEncoder (VQ-VAE)

326 **VQ-VAE network architecture** The *VQ-VAE* architecture (Oord et al., 2018) is formed of 3 parts: first, a convolutional  
 327 *encoder* compresses an input image  $x$  into a lower-dimensional representation  $z_e(x)$ , which is then *quantised* (by a nearest  
 328 329

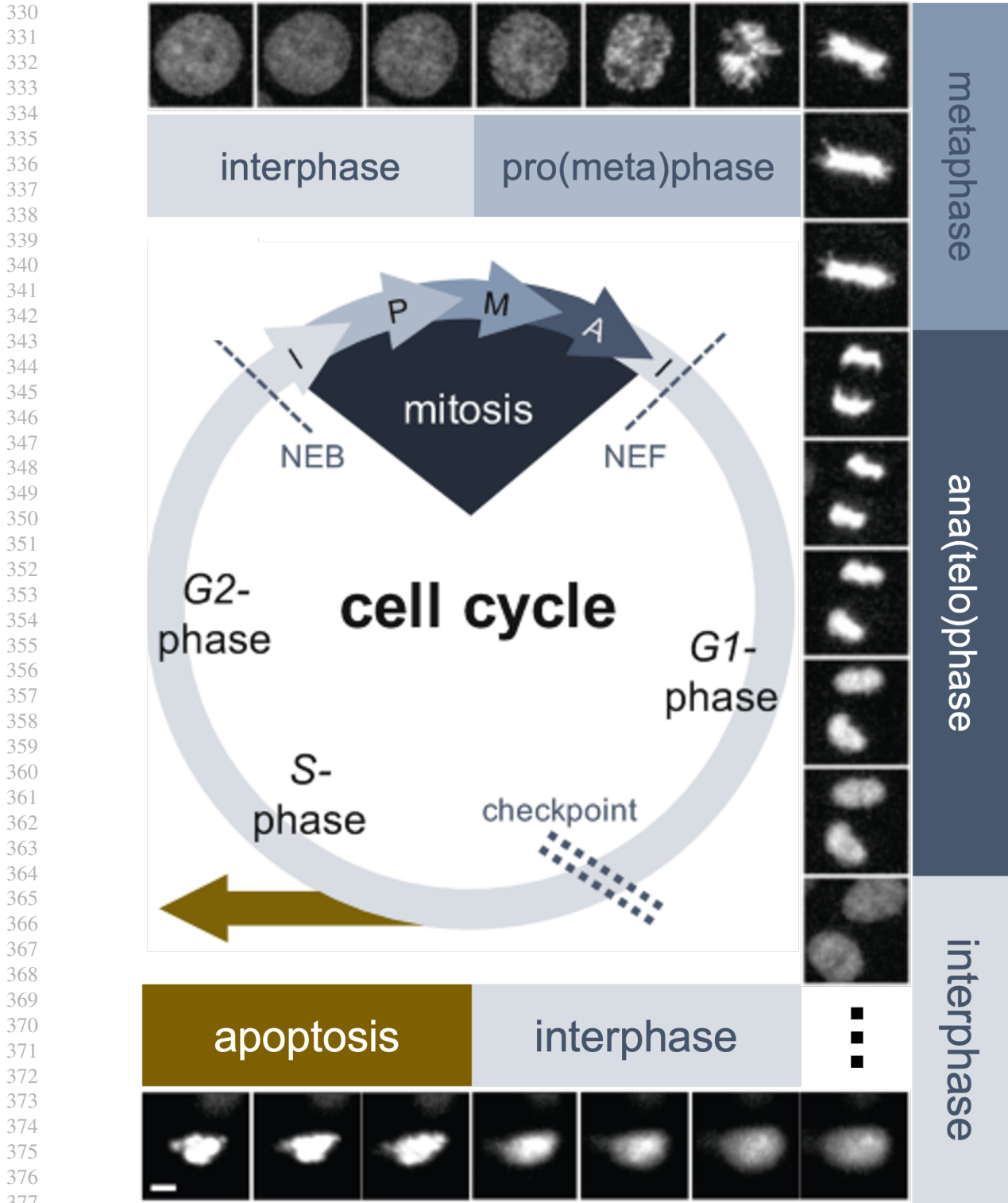


**Figure 8. Chromatin morphology during cell cycle.** Cell cycle progression with phase-specific changes to the H2B-GFP-labeled chromatin condensation level. Single-cell time-lapse image patches capturing the process from nuclear envelope breakdown (NEB) to nuclear envelope formation (NEF) are illustrated. During interphase, the G1, S, and G2 phases are separated by cell cycle checkpoints that regulate progression through the cycle; alternatively, the cell may escape the cell cycle temporarily, e.g. by becoming dormant or quiescent, or permanently, e.g. by undergoing apoptosis, or programmed cell death as illustrated. Images taken consecutively via time-lapse microscopy at frame rate = 4 minutes. Scale bar = 5  $\mu$ m. Adapted from (Ulicna et al., 2022).

neighbour look-up, or  $L_2$  norm) along the channel dimension to a “codebook”, *i.e.* an embedding space  $E \in \mathbb{R}^{K \times D}$ . Here,  $K$  is the size of the discrete latent space, *i.e.* the number of available embeddings  $e$  in the codebook dictionary, and  $D$  is the dimensionality of each latent embedding vector  $e_i$ . The quantised discrete embeddings  $z_q(x)$  are then passed through a convolutional *decoder* to produce the output image  $x'$ , which is the image reconstruction of the same dimensionality as the original input  $x$  (Fig.9).

**Objective function** The *VQ-VAE* overall loss function is composed of 3 terms:

$$\mathcal{L}(x, z) = \log p(x | z_q(x)) + \| \text{sg}[z_e(x)] - e \|_2^2 + \beta \| z_e(x) - \text{sg}[e] \|_2^2 \quad (1)$$

where the *reconstruction loss* (term 1) optimises both the encoder and the decoder of the model. In the forward pass, the nearest embedding  $z_q(x)$  is passed to the decoder, but the codebook embeddings receive no gradients due to discretisation bottleneck bypassing in the backward pass. The *embedding loss* (term 2) is then minimised via *vector quantisation* based on  $L_2$  distance, to move the embedding vectors  $e_i$  towards the encoder outputs  $z_e(x)$  by:

$$z_q(x) = e_k, \quad \text{where } k = \text{argmin}_j \| z_e(x) - e_j \|_2 \quad (2)$$

Whilst this term only updates the codebook dictionary, the *commitment loss* (term 3) of  $z_e(x)$  to  $e$  prevents the dimensionless embedding space from growing arbitrarily. In addition,  $\beta = 0.25$  is the scaling constant to balance the reconstruction and commitment losses, which was found, together with other hyperparameters such as letting the model train for 10,000 iterations with an embedding size = 256 and dimensionality = 4 via hyperparameter search.

## B.2. Disentangled Beta Variational AutoEncoder ( $\beta$ -VAE)

**$\beta$ -VAE network architecture** A convolutional variational autoencoder was built to learn a low-dimensional, interpretable representation of the cell image data. The VAE is based on an encoder-decoder network crosstalk through a low-dimensional bottleneck - called the latent representation. The encoder part of the network is convolutional in nature, transforming the single-depth input patch  $\mathbf{x}$  from the image space to the latent space. The dimensionality of the latent representation is specified in a separate hyperparameter. The decoder part of the network takes the latent mean of each feature in the representation and performs a series of reciprocal transformations to convert it back to an image space, yielding an reconstruction image,  $\mathbf{x}'$  (Fig.9).

The encoder network consisted of four convolutional layers with  $3 \times 3$  kernels with 32, 64, 128 and 256 kernels, respectively, and Swish activation functions to introduce non-linearity. Each layer was pooled by a max-pooling operation with  $2 \times 2$  pool size and stride. The convolutional output was flattened and passed through two FC layers with 256 units each - and swish activations - before being split into two branches - one FC layer branch was allowed to learn the mean, or  $\mu$ , and the other one learned the variance, or  $\sigma^2$ , estimator. For the Gaussian reparametrisation trick, a random normal sampler was used to generate samples from the distribution. The architecture of the decoder is the inverse of that of the encoder, using nearest-neighbour upsampling between convolutional layers (Fig.9).

**Objective function** The following objective function was used to train the network (Burgess et al., 2018; Higgins et al., 2017):

$$\mathcal{L}(\theta, \phi; \mathbf{x}, \mathbf{z}, \gamma, C) = \mathbb{E}_{q_\phi(\mathbf{z}|\mathbf{x})} [\log p_\theta(\mathbf{x}|\mathbf{z})] - \gamma |\text{D}_{\text{KL}}(q_\phi(\mathbf{z}|\mathbf{x}) || p(\mathbf{z})) - C| \quad (3)$$

This loss function is composed of two competing terms. The combination of these two terms pushes the  $\beta$ -VAE to learn reliable representations of the image data, while regularising the latent space to promote a continuous representation of its latent space. Namely, the two components are:

1. The **reconstruction** component, which penalises differences between the original input image,  $\mathbf{x}$ , and the reconstructed output image  $\mathbf{x}'$ . The mean squared error (MSE) function is implemented for the reconstruction loss.
2. The **regularisation** component, which implements the Kullback-Leibler divergence ( $\text{D}_{\text{KL}}(\cdot || \cdot)$ ). The aim of this is to penalise the latent space model variance from dropping to zero. This is done by forcing the encoding to match the prior distribution, here defined as a Gaussian prior with a diagonal covariance matrix,  $N(0, I)$ .

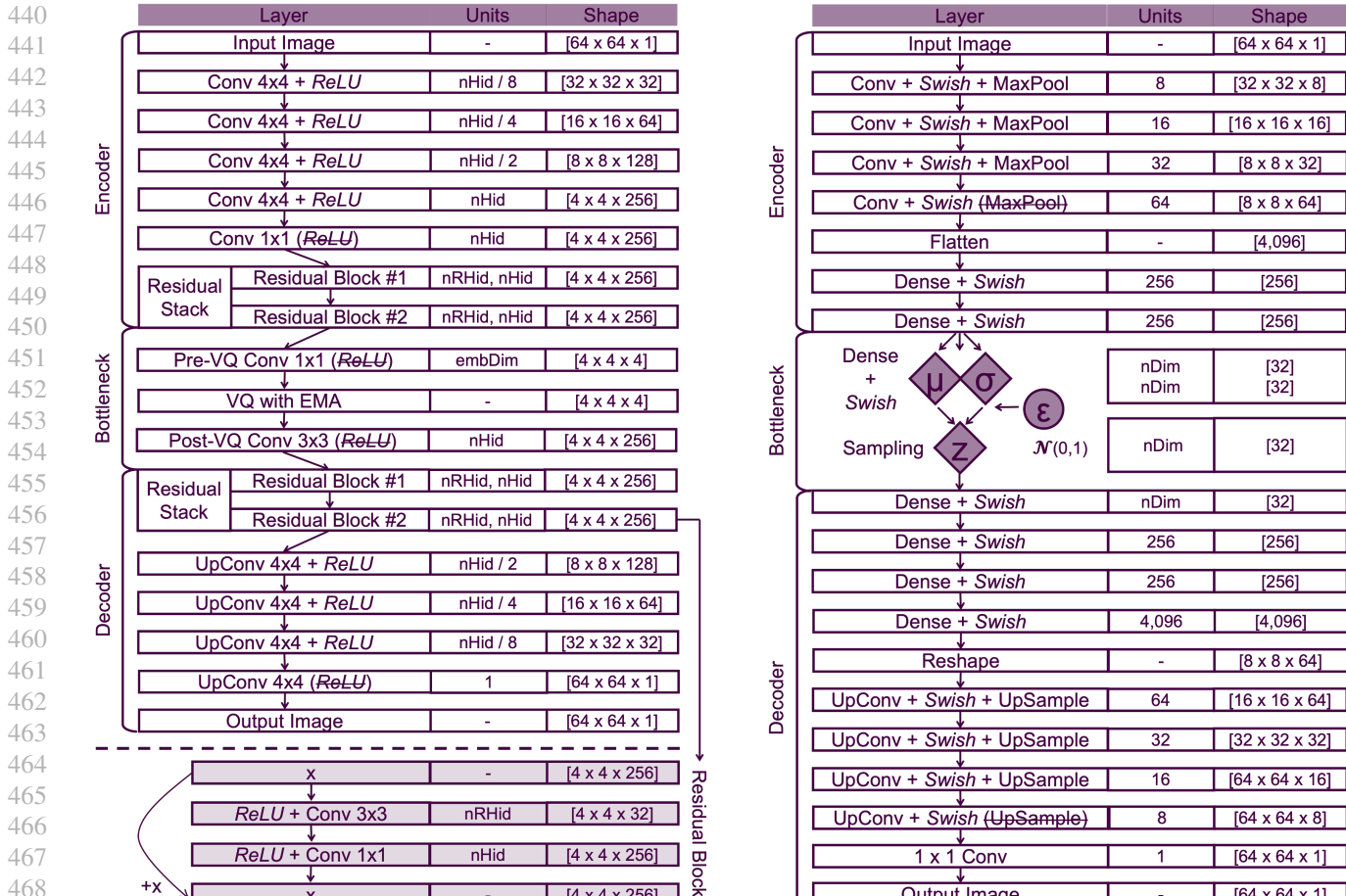


**Figure 9. Architecture of the VQ-VAE (left) and  $\beta$ -VAE (right) models.** **VQ-VAE model architecture:** The normalised single-channel input is funnelled through five convolutional layers, the output of which is flattened before being fed through a residual stack (illustrated at the bottom). The output of the residual stack is then fed into an additional convolutional layer to match the data dimensionality for the bottleneck where vector quantisation is performed. The entire process is reversed at the exit from the bottleneck and in the decoder step, to generate an output image with the identical dimensionality to the input image, [64, 64, 1]. Where (Up)Conv is specified, it suggests that an (up-)convolution 2D was performed with 2D *kernel\_size* of  $4 \times 4$  and stride of 2, or stride of 1 otherwise (kernel sizes  $3 \times 3$  and  $1 \times 1$ ). Rectified Linear Unit (ReLU) was used as an activation function throughout the architecture, and excluded at particular points to allow the downstream tensor to carry negative values (VQ-step, entry to residual stacks, output image). VQ, vector quantisation; EMA, exponential moving average; nHid, number of hidden units; nRHid, number of hidden units in the residual block; embDim, dimensionality of the embedding vector;  $+x$ , element-wise addition of original input (identity operation).  **$\beta$ -VAE model architecture:** The normalised single-channel input is funnelled through four convolutional layers, the output of which is flattened before being fed through two fully-connected (dense) layers. Then, the output is split into two separate dense layers, which represent the mean ( $\mu$ ) and log variance ( $\sigma$ ) estimators of the distribution with specified dimensionality (here, 32). The  $\mu$  and  $\sigma$  vectors are sampled from in the next layer using the Gaussian reparametrisation trick where  $z = \mu + \sigma \times \epsilon$  where  $\epsilon \sim \mathcal{N}(\mu, \sigma)$ . This step separates the learnable (deterministic, diamond-shaped) parameters from the stochastic (circle) node to allow gradient flow during backpropagation. This randomly sampled information is then processed until the final layer, whose output is the same shape as the input. The final convolutional layer features  $1 \times 1$  kernel that does not alter the image dimensions and omits the *Swish* activation function to allow the output to contain real negative pixel values. The decoder layers use nearest neighbour up-sampling between the convolutional layers to reverse the effect of the max-pooling layers in the encoder. For illustration, 32-dimensional space is used in the bottleneck step.

The bottleneck capacity ( $C$ ) of the network was dynamically adjusted during training. The value of  $C$  was scaled linearly as a function of training iteration, eventually reaching a maximum value  $C_{\max}$  at 90% of training progression, remaining at the maximum plateau phase for the final epochs. This ensures that at early training iterations the network prioritise the encoding (through the regularisation loss), while at later iterations this is refined to optimise the decoding (through the reconstruction loss). The scaling constant  $\gamma$  balances the two terms of the loss function.

---

**B.3. Pre-trained Residual Connection Network (ResNet)**

The PyTorch implementation of the ResNet-18 model (He et al., 2015) was used as an “off-the-shelf” feature extractor with default weights pre-trained on ImageNet dataset<sup>1</sup>. The initial layer was modified to input a single-channel image and resize it to  $224 \times 224$  pixel patch. The last layer was removed from the architecture, and the 512 features-long vector from the penultimate layer was used for the subsequent warping.

**C. Appendix: Dynamically warping time series latents**

**Distance metric** An Euclidean ( $\ell_2$ ) distance between two  $L$ -dimensional vectors (in this case, two image embeddings) is generalised as:

$$D_E(\mathbf{a}, \mathbf{b}) = \sqrt{\sum_{i=1}^L (b_i - a_i)^2} \quad (4)$$

where  $\mathbf{a}$  and  $\mathbf{b}$  are the Cartesian vectors starting from the space origin,  $a_i$  and  $b_i$  are two points in Euclidean space where  $\mathbf{a}, \mathbf{b} \in \mathbb{R}^L$ .

**Dynamic time warping (DTW)** First, a pairwise cumulative warping matrix is computed (using Eq. 4) between any two trajectories. This matrix can be used to find the shortest DTW alignment path between the sequences of (non-)identical length using dynamic programming.

Two vectors  $t$  and  $r$  of lengths  $m$  and  $n$ , respectively, are found a mapping path  $\{(p_1, q_1), (p_2, q_2), \dots, (p_k, q_k)\}$  such that the distance on this mapping path  $\sum_{i=1}^k |t(p_i) - r(q_i)|$  is minimized. In backward DTW, the optimum-value function is defined as  $D(i, j)$  as the DTW distance between  $t(i : m)$  and  $r(j : n)$ , with the mapping path from  $(i, j)$  to  $(m, n)$ . This recursively traverses the path as follows:

$$D(i, j) = |t(i) - r(j)| + \min \left\{ \begin{array}{c} D(i+1, j) \\ D(i+1, j+1) \\ D(i, j+1) \end{array} \right\} \quad (5)$$

with the initial condition  $D(m, n) = |t(m) - r(n)|$  and the final answer of  $D(1, 1)$  (Berndt & Clifford, 1994).

---

<sup>1</sup><https://pytorch.org/vision/main/models/generated/torchvision.models.resnet18.html>